# Chapter 3
# Electrocatalysis of Formic Acid Oxidation

**Cynthia Ann Rice and Andrzej Wieckowski**

**Abstract** Direct liquid fuel cells for portable electronic devices are plagued by poor efficiency due to high overpotentials and accumulation of intermediates on the electrocatalyst surface. Direct formic acid fuel cells have a potential to maintain low overpotentials if the electrocatalyst is tailored to promote the direct electrooxidation pathway. Through the understanding of the structural and environmental impacts on preferential selection of the more active formic acid electrooxidation pathway, a higher performing and more stable electrocatalyst is sought. This chapter overviews the formic acid electrooxidation pathways, enhancement mechanisms, and fundamental electrochemical mechanistic studies.

## 3.1 Introduction

The ever-increasing energy demands of portable electronic devices have overburdened the power supply capabilities of today's state-of-the-art battery technologies. The markets for small personal electronic devices are driven by three dominant criteria: (1) reduced volume, (2) decreased weight, and (3) increased uninterrupted power. Batteries are essentially "energy storage devices" due to their finite storage capacity that scales with energy density. Fuel cells are potentially a competitive alternative to batteries, promoting efficient conversion of chemical energy directly to electrical energy. Fuel cells are capable of "hot" refueling, permitting 24/7 operation. For personal portable electronic devices, based on current

C.A. Rice (✉)
The Center for Manufacturing Research, Department of Chemical Engineering, Tennessee Tech University, Cookeville, TN 38505, USA
e-mail: criceyork@tntech.edu

A. Wieckowski (✉)
The University of Illinois at Urbana-Champaign, Urbana, IL 61801, USA
e-mail: awieckow@illinois.edu

M. Shao (ed.), *Electrocatalysis in Fuel Cells*, Lecture Notes in Energy 9,
DOI 10.1007/978-1-4471-4911-8_3, 

fuel cell technologies, proton exchange membrane fuel cells (PEMFC) using direct liquid fuel-oxygen (anode/cathode) are currently the most viable, meeting criteria 1 and 2 above.

High sustainable power densities demanded by criterion 3 remains a challenge. Anode fuel type and catalyst selection are pivotal in attaining high overall conversion efficiencies and power densities. Hydrogen fuel is capable of high conversion efficiencies, but for portable devices the requirement of onboard compressed gas storage or reforming has negative implications to criteria 1 and 2. Direct liquid fuel cells (DLFC) have the advantages of easy transport and handling but typically suffer from poor conversion efficiencies, high fuel crossover through the PEM, toxicity, and poor leak detection [1]. Direct formic acid fuel cells (DFAFC) overcome several of the issues of DLFCs, having low fuel crossover, low toxicity, and a putrid odor for fast leak detection. The first DFAFC was demonstrated in 1996 on a phosphoric acid-doped polybenzimidazole (PBI) membrane at 170 °C [2]. In the early 2000s, Masel et al. began working on DFAFCs with Nafion™ (sulfonated tetrafluoroethylene) membranes, operating below 60 °C [3–10]. A drawback of DFAFCs in terms of liquid fuels is the low volumetric energy density of formic acid (2,104 Wh $L^{-1}$) as compared to methanol (4,900 Wh $L^{-1}$). This deficiency in DFAFCs is compensated by the 6× reduction in crossover through the Nafion™ membrane, allowing substantially higher fuel concentrations—5 to 12 M formic acid versus only 1–2 M for methanol [9, 11, 12]. For a formic acid-oxygen fuel cell, the theoretical open circuit voltage (OCV) is 1.48 V at 25 °C determined from the formal potentials of the anode and cathode half-cell reactions, respectively ($E_{cell} = E_{cathode} - E_{anode} = 1.23\ V - (-0.25\ V) = 1.48\ V$). The theoretical OCV for formic acid is larger than either hydrogen or direct methanol fuel cells: 1.23 V and 1.21 V, respectively. The magnitude of parasitic overpotentials and conversion efficiencies for formic acid electrooxidation are dependent on catalyst composition and size since they dictate the dominant reaction pathways.

(All cited potentials are versus a reversible hydrogen reference electrode (RHE) unless otherwise stated.)

Formic acid is produced in nature (biofuels), commercially, and as a byproduct of commercial synthesis. Renewable, carbon neutral, synthesis processes are also under investigation to form formic acid from $CO_2$ [13]. Reagent grade formic acid requires further purification to remove ppm levels of common substituent impurities, i.e., methyl formate, methanol, and acetic acid [14].

## 3.2 Review of Reaction Pathways

Since around 1960, the formic acid electrooxidation mechanism has been investigated, resulting in several review articles [15–18]. Formic acid electrooxidation studies have been carried out on pure metal electrodes, such as platinum (Pt) [19], palladium (Pd) [20], gold [21–23], rhodium [24, 25], and iridium [26]. Studies have also been performed on alloys, intermetallics, and adatoms. The conversion efficiency is determined by the rate of a series of steps: (a) reactant adsorption, (b) electrooxidation, and (c) product desorption. The electrooxidation

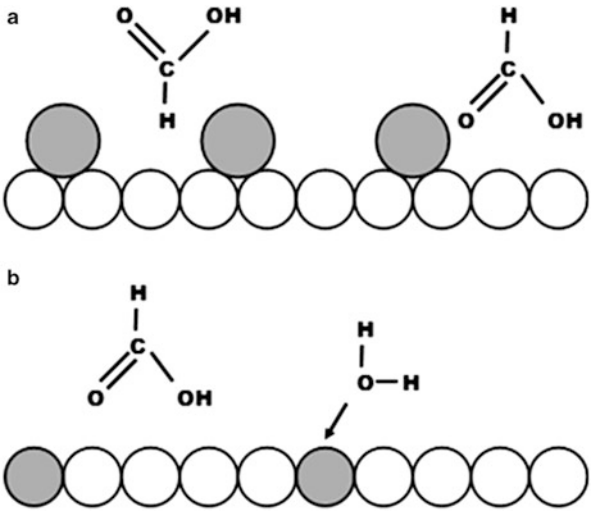


**Fig. 3.1** Catalyst-mediated formic acid electrooxidation mechanisms: (**a**) ensemble/third-body effect and (**b**) bifunctional mechanism. The catalyst atoms: (*open circle*) commonly Pt or Pd and (*filled circle*) secondary metal atom

pathway selection (step b) is controlled by the initial adsorption orientation of formic acid either in the CH-down or CH-up configuration (step a; see Fig. 3.1a) [27–29]. The subsequent electrooxidation (step b) occurs via either a dual [30] or triple [19, 31] pathway mechanism: the direct dehydrogenation and the indirect dehydration reactions. It has been suggested by Behm et al. [19, 31] and Osawa et al. [32, 33] that a third reaction pathway through a bridge-bonded formate ($HCOO_{ad}$) intermediate is possible. Their attenuated total reflection Fourier transform infrared (ATR-FTIR) spectroscopic measurements demonstrated a fast formate "adsorption–desorption equilibrium," limiting appreciable formate conversion to $CO_2$ [19, 31].

The direct dehydrogenation pathway favors high turnover efficiencies at low overpotentials through a direct conversion of formic acid to the carbon dioxide ($CO_2$) product [Eq. (3.1)]:

$$\mathrm{HCOOH} \rightarrow \text{active intermediate} \rightarrow \mathrm{CO_2} + 2\mathrm{H^+} + 2e^- \tag{3.1}$$

Alternatively, the indirect dehydration pathway forms a strongly adsorbed carbon monoxide ($CO_{ads}$) reaction intermediate via an initial non-Faradic step [Eq. (3.2a)]. To complete further oxidation of $CO_{ads}$, an additional activated hydroxyl species ($OH_{ads}$) is required. $OH_{ads}$ is typically formed on a separate catalytic surface site [Eq. (3.2b)] at higher overpotentials. The two adsorbed intermediates diffuse across the catalyst surface to combine and complete the conversion sequence [Eq. (3.2c)]. The limited availability of $OH_{ads}$ results in the accumulation of $CO_{ads}$ that blocks the catalyst surface, limiting the turnover efficiency [34, 35]:

$$\mathrm{HCOOH} + \mathrm{M(1)^0} \rightarrow \mathrm{M(1)–CO_{ads}} + \mathrm{H_2O} \tag{3.2a}$$

$$\mathrm{M(2)^0} + \mathrm{H_2O} \rightarrow \mathrm{M(2)–OH_{ads}} + \mathrm{H^+} + e^- \tag{3.2b}$$

$$\mathrm{M(1)–CO_{ads}} + \mathrm{M(2)–OH_{ads}} \rightarrow \mathrm{M(1)^0} + \mathrm{M(2)^0} + \mathrm{CO_2} + \mathrm{H^+} + e^- \tag{3.2c}$$

Typically, the metals (M) that participate in either electrooxidation reactions (3.2a) or (3.2b) in the dehydration pathway to form $CO_{ads}$ [Eq. (3.2a)] and $OH_{ads}$ [Eq. (3.2b)] at low overpotentials are not the same, completing the electrooxidation reaction through a complementary bifunctional mechanism [36]. The dual M catalysts are either comprised of alloys or adatoms. The overpotential of Eq. (3.2a) is low, as compared to formic acid's formal potential ($E_{anode}$). Unfortunately, the requirement of an activated $OH_{ads}$ species imposes a penalty on the conversion efficiency through overpotentials exceeding 0.3 V even on ruthenium (Ru) surface sites. For formic acid electrooxidation, the dominance of one reaction pathway versus the other is dependent on the physical and electronic characteristics of the catalyst, thus catalyst optimization is pivotal in reducing overpotentials by promoting the dehydrogenation pathway [Eq. (3.1)] and restricting accumulation of adsorbed reaction intermediates.

The presence of the dual pathway mechanism was experimentally verified in an elegant differential electrochemical mass spectroscopy (DEMS) study performed by Willsau et al. [37] (Fig. 3.2). Isotopically labeled $H^{13}COOH$ was oxidized at a polycrystalline Pt electrode at 0.25 V forming a partial surface coverage of adsorbed $^{13}CO$. While maintaining the potential, the solution was replaced with $H^{12}COOH$ followed by a positive potential scan to 1.5 V. The resulting DEMS response showed an immediate low potential loss of $^{12}CO_2$, followed by a combined $^{13}CO_2$ loss above 0.5 V. The presence of the $^{12}CO_2$ oxidation peak at voltages below 0.5 V confirms the presence of an alternative, less strongly adsorbed reaction intermediate because of the inability of Pt to activate $OH_{ads}$ required in the dehydration pathway [Eq. (3.2b)] at low voltages.

## 3.3 Enhancement Mechanisms

The catalytic enhancement mechanisms commonly described to facilitate the electrooxidation of hydrocarbon fuels are (a) the ensemble or third-body effect, (b) the bifunctional mechanism, and (c) the electronic effect [15, 16, 38]. Figure 3.1 shows a graphical description of (a) the third-body effect and (b) bifunctional mechanism. The third-body effect is typically attributed to enhancement of the dehydrogenation pathway by adatoms or alloys due to a steric hindrance facilitating preferential orientation of adsorbing formic acid in the CH-down direction, step (a) [27–29]. Alternatively, the dehydration pathway turnover frequency is accelerated by increased availability of activated hydroxyl groups [Eq. (3.2b)] at lower overpotentials through the bifunctional mechanism. Ultimately, the bifunctional mechanism is incapable of producing significant reductions in the overpotentials required for increased turnover efficiencies compared to the dehydrogenation pathway. The electronic effect could manifest itself either as a reduced $CO_{ads}$ bond strength or a preferential reactant adsorption orientation promoting the dehydrogenation reaction pathway.

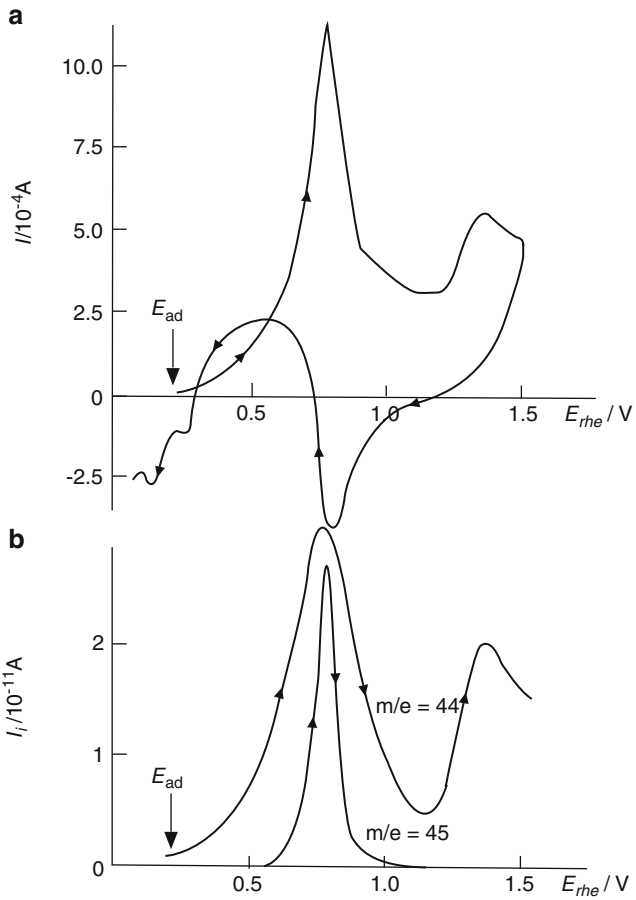


**Fig. 3.2** Formic acid cyclic voltammetry (**a**) coupled with differential electrochemical mass spectroscope (**b**) on Pt in 0.5 M $H_2SO_4$. Initially, $H^{13}COOH$ was pre-adsorbed at 0.25 V to form a sub-monolayer of Pt–$^{13}CO_{ads}$. After exchanging the solution with 10 mM $H^{12}COOH$, the voltage was scanned at 12.5 mV $s^{-1}$, resulting in an initial low-voltage mass signal for $^{12}CO_2$ ($m/e = 44$) via the dehydrogenation pathway and an additional signal for $^{13}CO_2$ due to the dehydration pathway [37]

## 3.4 Platinum and Palladium Electrocatalysts Reactivity

The electrooxidation of formic acid has been evaluated on single crystal, polycrystalline, unsupported nanoparticle and supported nanoparticle Pt- or Pd-based electrodes.

### *3.4.1 Single Crystal*

Formic acid electrooxidation has been studied on both Pt [39–41] and Pd [42] single-crystal surfaces. Herein we compare the work of Iwasita et al. [41] and Hoshi et al. [42] on Pt and Pd single crystals, respectively. The cyclic voltammograms were

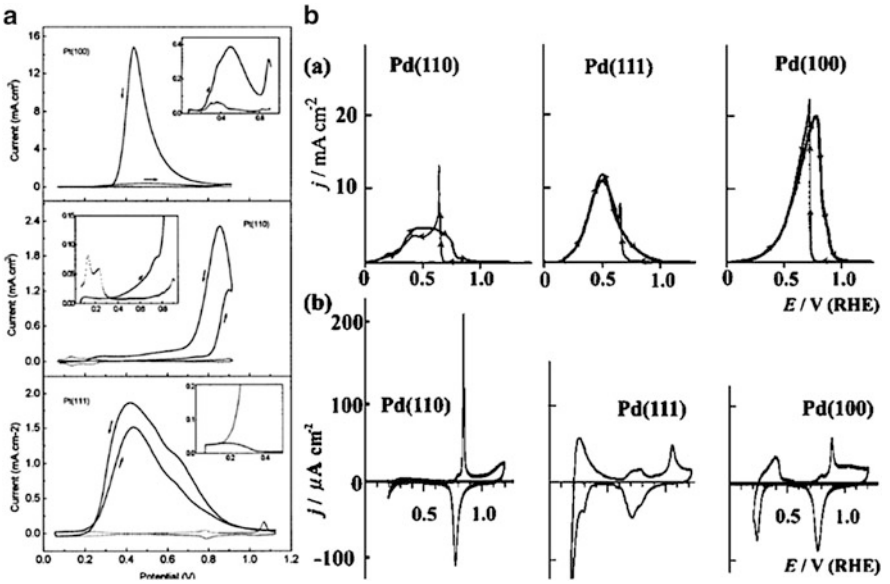


**Fig. 3.3** Single-crystal cyclic voltammograms of (**A**) Pt [41] and (**B**) Pd [42] for (110), (111), and (100) facets. The electrooxidation of 0.1 M formic acid is evaluated on the various faceted surfaces in 0.1 M $HClO_4$ supporting electrolyte at scan rates of 50 mV $s^{-1}$ and 20 mV $s^{-1}$, respectively. In (**A**) the *dashed lines* are for the background cyclic voltammograms of the different faceted Pd single crystals in 0.1 M $HClO_4$ alone, as are the designated (b) plots in (**B**) for Pt (reprinted with permission from [41] and [42], respectively)

performed under similar conditions, i.e., in 0.1 M $HClO_4$ supporting electrolyte solution and 0.1 M formic acid at room temperature. On the three types of single crystals studied (Fig. 3.3), the formic acid electrooxidation reaction pathway is impacted by (a) competitive adsorption of both hydrogen and oxygen, (b) availability of adsorbed oxygen, and (c) shifting of the d-band centers of the metal surface atoms due to changes in the interatomic bond lengths. The portion of the cyclic voltammograms most relevant to fuel cell operations is the low-voltage anodic sweep, <0.4 V.

Selecting 0.4 V vs. RHE as a potential relevant to operating DFAFCs, Pt has the following anodic scan single crystal orientation dependence: Pt(110) 0.015 mA $cm^{-2}$ < Pt(100) 0.31 mA $cm^{-2}$ < Pt(111) 1.8 mA $cm^{-2}$ [41]. The overall performance at 0.4 V on Pd single crystals is higher than that of Pt, with preference on different facets: Pd(100) 2.7 mA $cm^{-2}$ < Pd(110) 4.5 mA $cm^{-2}$ < Pd(111) 8 mA $cm^{-2}$ [42]. The symmetry between the forward anodic and reverse cathodic sweep currents is similar for all Pd single-crystal electrodes and asymmetric for Pt with the cathodic sweep current significantly higher than that of the anodic. Formic acid electrooxidation on both Pt and Pd is suppressed at the higher potentials during the anodic sweep due to competitive adsorption of $OH_{ads}$ blocking the surface sites on both catalyst types. The Pd cyclic voltammogram profile supports the dominance of the dehydrogenation pathway on all facets. The lack of significant current densities in the anodic sweep

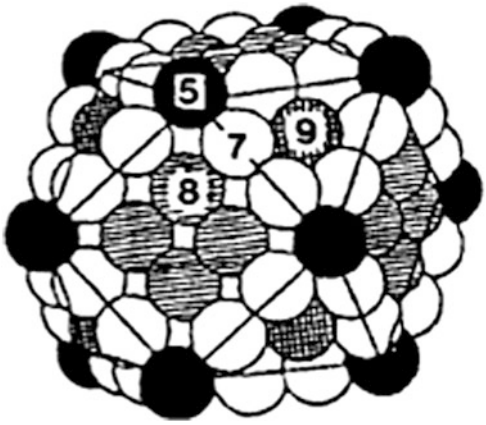


**Fig. 3.4** Cuboctahedral nanoparticle (~1.5 nm). Types of surface atoms corner (*filled circle*), edge (*open circle*), and terrace (*hashed circle*). The numeric values represent the coordination of adjacent atoms [43]

for both Pt(100) and Pt(110) suggests the increase propensity of the dehydration pathway on these surface. For the Pt(100) surface, the current density response is asymmetric with relatively little activity in the anodic sweep and an amplified intensity exceeding that of the other two facets in the reverse sweep.

### *3.4.2 Nanoparticle: Size Effect*

The electrooxidation of formic acid is a heterogeneous reaction involving only surface atoms, thus it is cost effective to reduce the particle size, increasing the dispersion (ratio of the number surface atoms to the total number of atoms) of the catalyst. As particle size decreases, the relative abundance of corners and edges increases, accompanied by a decrease in extended surface terraces that results in undercoordinated catalysts with altered d-band energetic and interatomic lattice spacing; all of which are potentially negatively impacting specific activity (current per unit surface area). Metal nanoparticles are typically described by a cuboctahedral geometry, shown in Fig. 3.4 [43]. Nanoparticle sizes below 10 nm require stabilization by an electrically conducting support (typically carbon) introducing possible metal–support interactions.

Park et al. compared methanol versus formic acid electrooxidation on polycrystalline Pt and on two sizes of carbon-supported Pt (2.0 nm vs. 8.8 nm) (Fig. 3.5) [44]. The potentials were referenced to a saturated calomel electrode (SCE) (RHE, 0.242 V) in 0.05 M $H_2SO_4$ at a scan rate of 50 mV $s^{-1}$. The cyclic voltammograms were normalized to a 1 $cm^2$ Pt "effective area." They observed a reduction in methanol activity for particles smaller that 4 nm and an opposite effect for formic acid; see Fig. 3.5. The disparity between methanol and formic acid size-dependent performance trends is due to methanol preferentially adsorbing onto three adjacent Pt atoms found on Pt(111)-faceted surfaces during the C–H bond dissociation step

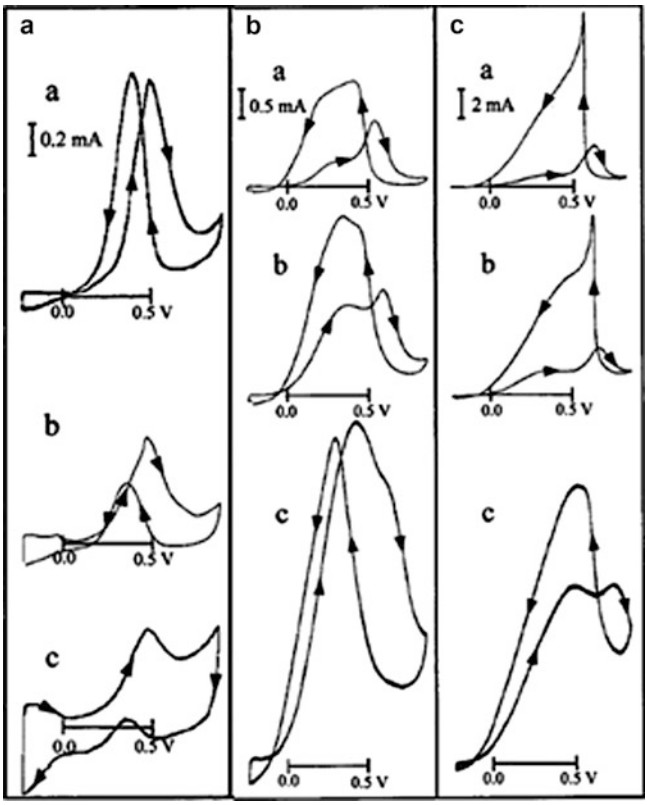


**Fig. 3.5** Cyclic voltammograms on (a) polycrystalline Pt, (b) Pt(8.8 nm)/C, and (c) Pt(2.0 nm)/C in 0.05 M $H_2SO_4$ at 50 mV $s^{-1}$ versus SCE. Electroactive species in solution (**A**) 0.01 M methanol, (**B**) 0.01 M formic acid, and (**C**) 0.1 M formic acid. The active surface area of each electrode was measured in pure electrolyte solution and normalized to 1 $cm^2$ Pt (modified from Park et al. [44])

to form $CO_{ads}$ [45]. Adzic et al. attributed these differences to a facet-dependent bond strength for the adsorbed methanol intermediate [40]. As particle size decreases, the number of adjacent surface sites needed for adsorption decreases resulting in a decrease in the maximum current density. Additionally, the available surface sites are further diminished by $OH_{ads}$ at elevated potentials, resulting in a reduction in methanol adsorption onto the catalyst surface during the reverse potential sweep.

Formic acid adsorption onto Pt requires either multiple sites for the dehydration pathway or only one to activate C–H bond for the dehydrogenation pathway [46]. The onset of formic acid electrooxidation has been shown to be effected by both Pt particle size and reactant concentration (Fig. 3.5B, C). The dehydration pathway is favored on both the polycrystalline and 8.8 nm Pt catalyst surfaces during the forward scan, as is apparent from the low currents and high overpotentials. The higher potentials are required to form the activated hydroxyl complexes required to oxidize the passivating CO moieties to $CO_2$, similar to methanol. The formic acid

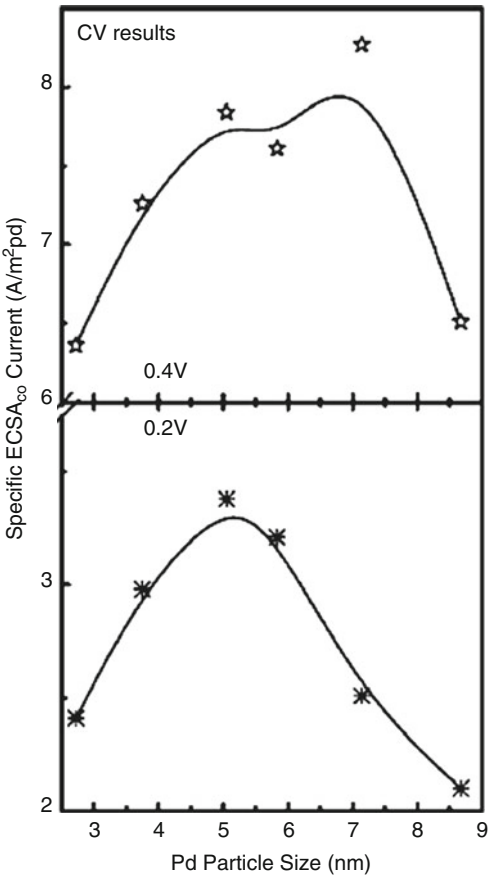


**Fig. 3.6** Size-dependent current densities acquired at (**A**) 0.4 V and (**B**) 0.2 V versus RHE from cyclic voltammograms anodic scan (5 mV $s^{-1}$) on carbon-supported Pd nanoparticles (Pd/C) in 3 M formic acid and 0.1 M $HClO_4$ [48]

electrooxidation rate on the 2.0 nm Pt nanoparticles is significantly enhanced, resulting in reduced overpotentials during the forward scan. The authors attribute this to the reduction in the abundance of contiguous terrace binding sites promoting the dehydrogenation reaction pathway. The maximum current was higher in 0.1 M formic acid (Fig. 3.5C), but the onset potential was unexpectedly shifted to higher overpotentials for the reaction to proceed.

On Pd catalyst, the dehydrogenation pathway is dominant at low overpotentials in the positive scan [30, 47]. The Pd particle size dependence of formic acid electrooxidation was studied by Zhou et al. with carbon-supported nanoparticles (SA = 240 $m^2$ $g^{-1}$) ranging from 2.7 to 9 nm [48]. In this study, X-ray photoelectron spectroscopy was used to decouple the particle size effects on the surface binding energy and corresponding valency of the Pd species ($Pd^0$, $Pd^{2+}$, and $Pd^{4+}$). As the particle size decreased, the $Pd^0$ surface species was reduced by a factor of 2 and the $Pd^{2+}$ increased by a third. The $Pd^{4+}$ was observed at low percentages for particles under 4 nm. The formic acid cyclic voltammograms support the dominance of the dehydrogenation pathway on the Pd nanoparticle catalysts. As shown in Fig. 3.6, the most active Pd/C size is (a) around 6.5 nm at 0.4 V but (b) only 5.2 nm at 0.2 V versus RHE in 3 M formic acid and 0.1 M $HClO_4$.

Although Pd has superior initial performance at low overpotential, it is quickly deactivated over time. Pan et al. from Tekion Inc. showed that at 40 °C in a DFAFC environment 30 % of the power was lost in the first 3 h of operation [49]. The degradation is attributed to the accumulation of $CO_{ads}$-like species on the Pd nanoparticle surface during continuous operation [49–52]. Reactivation of the surface has been demonstrated by both electrochemical [49, 53, 54] and non-electrochemical [51] methods. This activity instability drives the search for more stable and active catalysts.

## 3.5 Modeling Insights

Several modeling efforts have been published probing the formic acid electrooxidation pathway mechanisms, specifically trying to quantify the energetics of each step [27, 28, 46, 55, 56]. Recent density functional theory (DFT) calculations by Neurock et al. and Wang et al. have shown the CH-down adsorption configuration results in a lower energy electrooxidation pathway of formic acid on Pt [28, 46]. In a recent theoretical study by Gao et al., the impact of the energetically favored formic acid electrooxidation pathways was probed due to the relative presence of water at the Pt(111) interface: (a) two water molecules versus (b) a bilayer network of water molecules [55]. They concluded that in the more realistic solvated environment, formic acid electrooxidation proceeds via a *dual-path mechanism* including the direct path with a transient $CO_2$*-adsorbed intermediate species and an indirect path that proceeds through an HCOO* species. Unfortunately, the models are for idealized planer single-crystal surfaces and are lacking connections to the more active nanoparticle surfaces—6.5 nm on Pd and 4 nm on Pt. To find the ideal catalyst structure to exclusively promote the dehydrogenation reaction, a firm relationship must be drawn between catalyst reactivity and physical atomic catalyst structure through the following sequence:

1. Surface solvation
2. Nanoparticle-faceted terraces, corners, and edges' presence
   (a) Third-body effect
3. Adatoms and alloying component addition
   (a) Third-body effect
   (b) Electronic effect
4. Surface coverage must be correlated to formic acid feed concentrations.
5. Impact of inner catalyst/ionomer agglomerate acidity.
6. $CO_2$ removal rate from the ionomer shell of the agglomerate.

In a relatively simple model by Leiva et al., the impact of adatom coverage in terms of a nearest-neighbor electronic effect versus a third-body effect was developed and compared to experimental results for both bismuth (Bi)- and antimony (Sb)-modified Pt single-crystal surfaces, shown in Fig. 3.7 [56]. One of

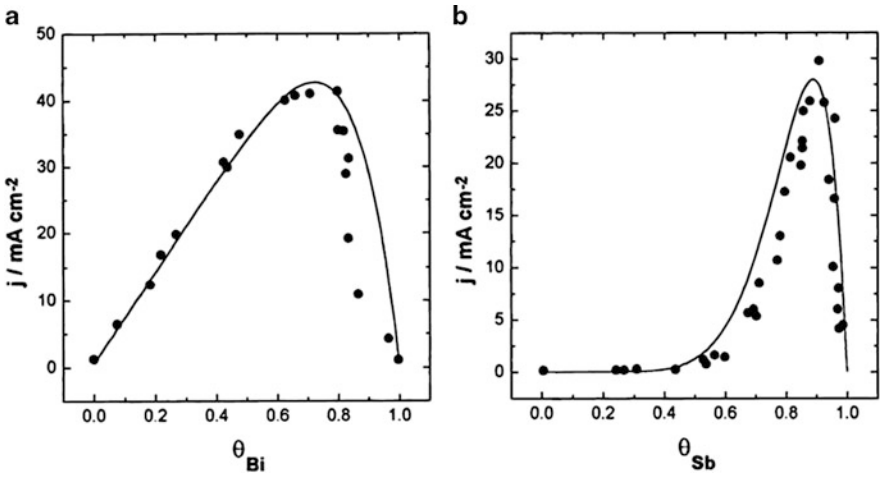


**Fig. 3.7** Adatom coverage-dependent current densities acquired at 0.5 V versus RHE from cyclic voltammograms anodic scan (50 mV $s^{-1}$) on Pt single-crystal electrodes in 0.25 M formic acid and 0.5 M $H_2SO_4$. The experimental results (*filled circle*) are compared to the theoretically (*continuous line*) predicted activity. (**A**) Pt(111)/bismuth and (**B**) Pt(100)/antimony [56]

the fundamental assumptions of the model was that formic acid only adsorbs onto Pt atoms. The experimental current density measurements were made at 0.5 V, 50 mV $s^{-1}$ in 0.25 M formic acid, and 0.5 M $H_2SO_4$. The different adatom surface coverages ($\theta$) resulted in significantly different current density trends. The addition of a slight fraction of Bi induced an immediate increase in performance, with a maximum between $\theta$ of 0.7 and 0.8. While the performance did not increase for Sb-modified surfaces until $\theta > 0.4$. The Bi enhancement was found to be consistent with an electronic effect proportional to the number of Bi–Pt pairs. The lack of impact at low coverages of Sb followed their predicted trend due to steric hindrance promoting CH-down adsorption through a third-body effect at elevated coverages.

Peng et al. combined electrochemical surface-enhanced infrared spectroscopy (EC-SEIRAS) and DFT calculations to probe the Sb adatom enhancement mechanism on polycrystalline Pt surfaces [27]. The forward cyclic voltammogram in 0.1 M formic acid and 0.5 M $H_2SO_4$ showed a 2.7× decrease in $CO_{ads}$ at potentials below 0.2 V versus RHE for a 0.6 monolayer (ML) Sb, with a tenfold current increase at 0.5 V in the forward scan. They concluded at coverages >0.25 ML that the $[Sb]^{\delta+}$ $[Pt]^{\delta-}$ dipole interaction enhances CH-down adsorption. This is consistent with Leiva et al.'s work presented above. They additionally attributed this coverage dependence to a decrease in the Pt–$CO_{ads}$ bond strength with increased Sb coverage.

Demirci investigated the degree of segregation and shifting of d-band centers by metal alloy combinations to improve the direct liquid fuel cell catalyst activity through electronic promotion of the dehydrogenation pathway [57]. He focused on Pt- and Pd-based catalyst for formic acid electrooxidation and looked at the potential impact of surface adatom adsorption of other 3d, 4d, and 5d transition metals. The criteria he imposed for improved catalytic activity on Pt and Pd

**Table 3.1** Comparison of shifts in d-band center (eV)/separation energies of ad-metals (impurities) to Pt and Pd

| | V | Cu | Nb | Pd | Ag | Ta | Pt | Au |
|---|---|---|---|---|---|---|---|---|
| Pt | /A1 | −0.33/n | /A2 | 0.19/A1 | 0.5/A2 | /A1 | 0 | 0.46/A2 |
| Pd | /S1 | /S1 | /A1 | 0 | 0.14/A1 | /S1 | −0.17/n | 0.17/A1 |

The separation energies are designated S for segregation, A for antisegregation, and n for no segregation—1, 2, and 3 as moderate, strong, and very strong, respectively [55]

surfaces were that the second metal did not segregate and a positive shift in the d-band center of Pt. The results from Demirci's work are listed in Table 3.1. The positive shift in the d-band center is predicted to enhance the adsorption of the "active intermediate" species [Eq. (3.1)]. Unfortunately, the relative d-band shifts were not provided for all the secondary metals of interest in Table 3.1. The Pd cross entries designated with S1 are predicted to segregate in the presence of the ad-metal. The predicted performance enhancement of Pd adatoms onto Pt and Au has been experimentally demonstrated by Wieckowski's group [6, 58–60]. Significant work has been preformed with gold (Au) incorporated onto both Pt and Pd catalyst, supporting Demirici's prediction [61–64].

## 3.6 Electrocatalyst Performance Studies

Controlled electrochemical experiments are designed to probe select aspects of the formic acid electrooxidation reaction as a function of material selection and/or experimental conditions. Unfortunately, the selected experimental technique employed imposes deviations from a complex three-dimensional catalyst layer used in an operational DFAFC and thus results in inconsistencies between techniques. Assuming the current–potential relationship is always directly correlated to Faraday's law for charge and $CO_2$ production, the assessment techniques can be broken down into three general categories: (1) indirect correlation, (2) desorbed product detection, and (3) direct catalyst surface analysis.

*General Electrochemical Setup*. Catalytic studies to probe formic acid electrooxidation efficiencies are commonly not performed in a complex fuel cell, but using a three-electrode electrochemical cell at room temperature, consisting of a working (catalyst of interest), a counter (Pt mesh), and a reference electrode. Potentials are typically referenced against an RHE, saturated calomel electrode (SCE), or silver/silver chloride (Ag/AgCl).

The supporting electrolyte type and concentration of formic acid impact the observed overpotentials. The two most commonly used supporting electrolytes are either $H_2SO_4$ or $HClO_4$. Specific bisulfate anion adsorption onto Pt surface sites from $H_2SO_4$ adversely increases the onset potential of formic acid electrooxidation. The top of Fig. 3.8 shows an unfavorable increase in the onset potential for $OH_{ads}$ in the anodic cycle by ~0.1 V on a Pt (~2.3 nm)/C catalyst in the presence of 0.1 M $H_2SO_4$ versus 0.1 M $HClO_4$ [65]. In the presence of 0.5 M formic acid, the initial response in the forward anodic sweep at potentials below 0.4 V versus SCE is

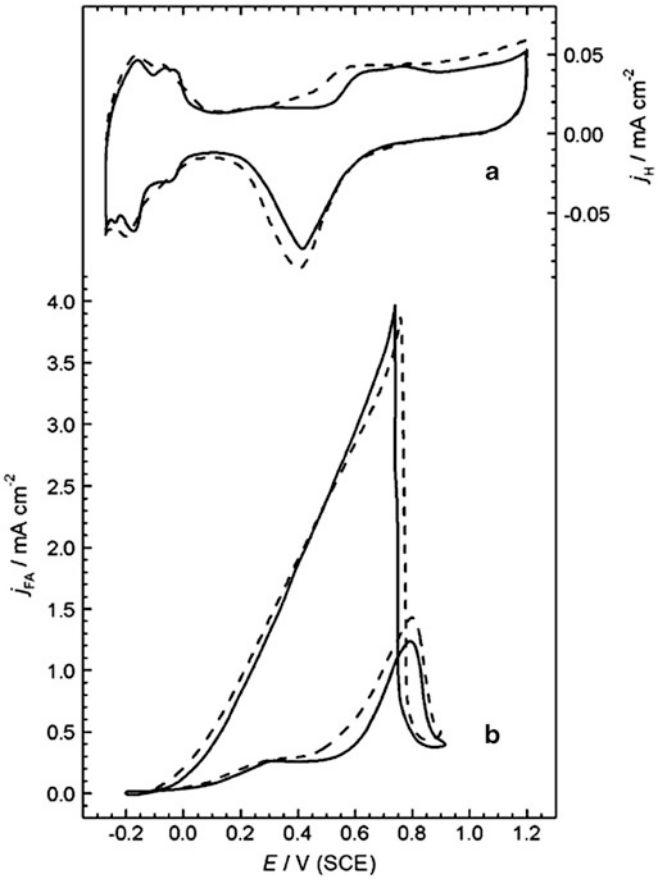


**Fig. 3.8** Comparison of cyclic voltammetric features in 0.1 M $H_2SO_4$ (*solid line*) and 0.1 M $HClO_4$ (*dashed line*) on Pt/C (47.5 wt% from Tanaka Precious Metal Group) at 50 mV $s^{-1}$. (**a**) Base electrolyte and (**b**) 0.5 M formic acid and base electrolyte [65]

relatively unaffected by the electrolyte. This may be attributed to the combined surface coverage of bisulfate and $CO_{ads}$ having relatively little impact on the availability of the single adsorption sites required for the dehydrogenation pathway. The onset and maximum current density for the second peak in the forward scan is negatively impacted by the presence of bisulfate.

The formic acid electrooxidation current density may be impacted by temperature, formic acid concentration, rotation rate of the working electrode (0–1,000 rpm), upper potential limit, and contamination from the reference electrode. The upper potential limit in the cyclic voltammogram, depending on catalyst type, impacts the magnitude of the reverse scan current density due to the promotion of the dehydration path through the formation of $OH_{ads}$ at higher potentials [66]. Masel's group has shown an increase in turnover efficiency of formic acid electrooxidation with increasing pH for both Pt and Pd catalyst [67].

Purity of the formic acid fuel can have significant effects on the initial and sustained catalyst performance. Commercial synthesis of formic acid contains residual precursors due to incomplete conversion or purification such as methanol, methyl formate, and formaldehyde [68]. In a recent paper by Law et al., the impact of ppm-level common catalyst poisoning substituents on steady-state DFAFC performance was investigated: methyl formate ($CH_3OC(O)H$), methanol, and acetic acid ($CH_3COOH$) [14]. At contamination levels of 50 ppm, an accelerated DFAFC decay at 200 mA $cm^{-2}$ was observed for all contaminates measured. To remove undesirable contaminates from the supplied standard commercial grade formic acid at minimal cost penalties, a patent from the Masel group demonstrates improved performance for formic acid pretreated by freeze distillation [68].

### 3.6.1 Indirect Correlation

Several types of indirect measurements may be used to infer the physical and/or chemical phenomena inducing changes in the formic acid electrooxidation activity. Using *in-vacuum* X-ray diffraction (XRD) and X-ray photoelectron spectroscopy (XPS) to complement electrochemical evaluations, Yu and Pickup have evaluated the change in electron density due to adatom addition of Bi [69] and Sb [70] individually onto Pt/C to assess coverage-dependent changes. Their results supported segregation of the adatom to the surface with no observable alloying.

*Electrochemical impedance spectroscopy* (EIS) is a powerful technique for probing reaction kinetics and mass transport limitations within a finite electrochemical system. EIS has been applied to both ex situ electrochemical cell [12, 71–76] and in situ fuel cell [11, 51, 77–79] formic acid systems. The discussion herein is limited to testing in a two-electrode electrochemical cell: electrode 1 (counter and reference electrodes)/electrode 2 (sense and working electrodes). The frequency range of interest is typically 10 kHz to 0.01 Hz at the acquisition interval of ten points per decade with an ac perturbation amplitude of 10 mV. The ac perturbation is superimposed upon a constant applied dc potential. The results are typically represented in a Nyquist plot, with the imaginary component ($-Z''$) versus the real component ($Z'$). The high-frequency intercept ($R_I$) is dominated by electrolyte resistance and contact resistance; in the electrochemical cell, these contributions are minimal and approach zero. The arc is a combination of charge transfer resistance ($R_{ct}$) and double-layer capacitance ($C_{dl}$). The $C_{dl}$ is represented in an equivalent circuit model as a capacitive phase element ($CPE_{dl}$) due to the impact of formic acid increasing the extent of solvation of ions across the Helmholtz layer [80]. Additional circuit elements may be included to account for electrooxidation of adsorbed reaction intermediate species. Mass transport resistances are typically not observed in a two-electrode electrochemical cell.

Wang et al. compared formic acid electrooxidation EIS Nyquist plots for Pt/C and PtPd(alloy)/C catalyst (Fig. 3.9a, b, respectively) [12]. The results were acquired in 0.5 M formic acid and 0.5 M $HClO_4$ over a range of applied dc potentials from 0.1 to 0.7 V versus Ag/AgCl (+0.199 V vs. RHE). The Nyquist

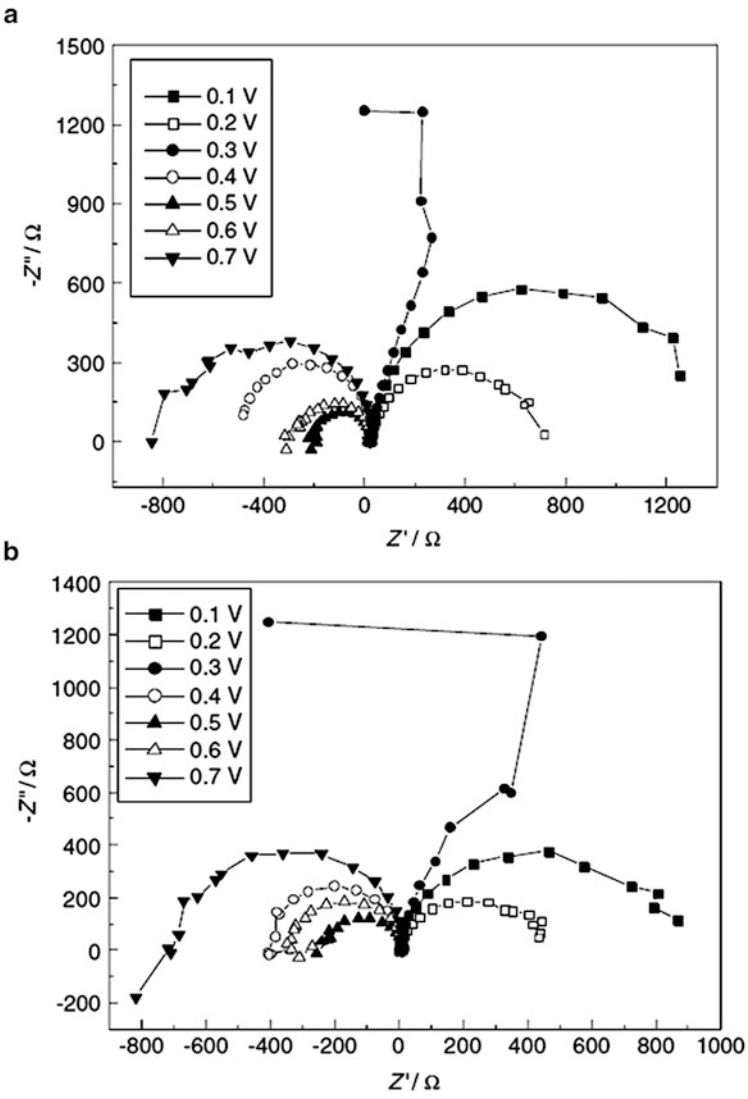


**Fig. 3.9** Nyquist plot of (**a**) Pt/C and (**b**) PtPd/C (alloy) at 25 °C in 0.5 M $HClO_4$ and 0.5 M formic acid as a function of applied potential [vs. Ag/AgCl/KCl(sat)] [12]

plots show activity in two quadrants, dependent on the applied potential and the dominant reaction mechanism. The arc in quadrant ($Z'$, $R_I \rightarrow +$) decreases as the potential is increased from 0.1 to 0.2 V for both catalyst types, which is consistent with a decrease in the $R_{ct}$ of the reaction. As the potential increases to 0.3 V, the radius of the arc increases beyond that observed for 0.1 V. The transitioning to the second quadrant ($Z'$, $R_I \rightarrow -$) has been attributed to the contribution of the dehydration reaction (3.2c), [12] being consistent with the anodic sweep of Wang's cyclic voltammograms (Fig. 10 in [12]) for the Pt/C and PtPd/C, which exhibited

similar peak trends with the activity of the PtPd/C catalyst and which is significantly higher for the identical applied potentials. The lower potential peak current below 0.5 V is attributed to the dehydrogenation reaction pathway, while the current from the dehydration pathway reaches a maximum between 0.6 and 0.8 V. Suo and coworkers studied Pd/C and attributed the increase in the arc in the second quadrant at higher applied potential to a blocking effect of surface oxide species [76]. Wang found that the $R_{ct}$ was smaller for the PtPd/C catalyst, but it followed the general trends of Pt/C in terms of arc location dependence on applied potential.

*Electrochemical quartz crystal microbalance*. To monitor adsorbate accumulation on catalyst surfaces from formic acid electrooxidation and advance mechanistic understanding, an electrochemical quartz crystal microbalance (EQCM) can be used to simultaneously measure current and mass [22, 66, 81–83]. The dampening of the vibration frequency ($\Delta f$ ) of an AT-cut 9 MHz piezoelectric crystal is directly proportional to mass accumulation ($\Delta m$) on the catalyst surface through the Sauerbrey equation $(\Delta f = -f_0^2 2(\mu_q \rho_q)^{-1/2} \Delta m/A)$ [84], where $f_0$ is the base frequency, $\mu_q$ is the quartz shear modulus, $\rho_q$ is the density of the quartz, and $A$ is the active area. The detection limit can be as low as $\pm 0.4$ ng cm$^{-2}$ [85].

In a three-electrode electrochemical arrangement, in the absence of formic acid, the $\Delta m$'s on polycrystalline Pt working electrodes during potential cycling are associated with H-adsorption–desorption, double-layer alignment, and oxide formation/reduction [85]. In the presence of 0.1 M formic acid and 0.2 M $HClO_4$ at 50 mV s$^{-1}$, Tian and Conway observed competitive adsorption between $CO_{ads}$ [Eq. (3.2a)] and $Ox_{ads}$ [Eq. (3.2b)] formation [66]. They observed strong symmetry between the current- and mass-dependent potential response on the forward anodic sweep. Figure 3.10 shows the effect of sequentially increasing the upper potential limit (0.6–1.4 V vs. RHE) during cyclic voltammetric measurements (from 0.05 V) on the (a) current and (b) mass response in 0.2 M $HClO_4$ and 0.2 M formic acid [66]. *Positive scan*—The forward anodic scan is unaffected by the previous upper potential limit. As the potential increases in the positive direction, the emergence of a second peak with a maximum current at 1.05 V is observed without a corresponding increase in mass (decrease in frequency); this observation is attributed to the favorable autocatalytic low oxide layer coverage facilitating step 3 [Eq. (3.2c)] in the indirect reaction pathway. Above 1.05 V the mass increases which corresponds to the accumulation of an oxide layer on the Pt surface and inhibition of formic acid adsorption. The growth of an oxide layer is shifted by about 200 mV in the presence of formic acid. *Negative scan*—While the reverse negative going scan shows a strong dependence on the upper potential limit, when the potential is limited to less than 0.8 V, the current in the reverse scan is only slightly higher than that in the forward scan; the current peak near 0.6 V shifts to higher potentials with increasing upper potential limits. A distinct current spike is observed for upper potential limits of 1.05 V and greater which coincides with the increase in mass due to surface oxide accumulation. As the surface oxide layer becomes more well developed at higher

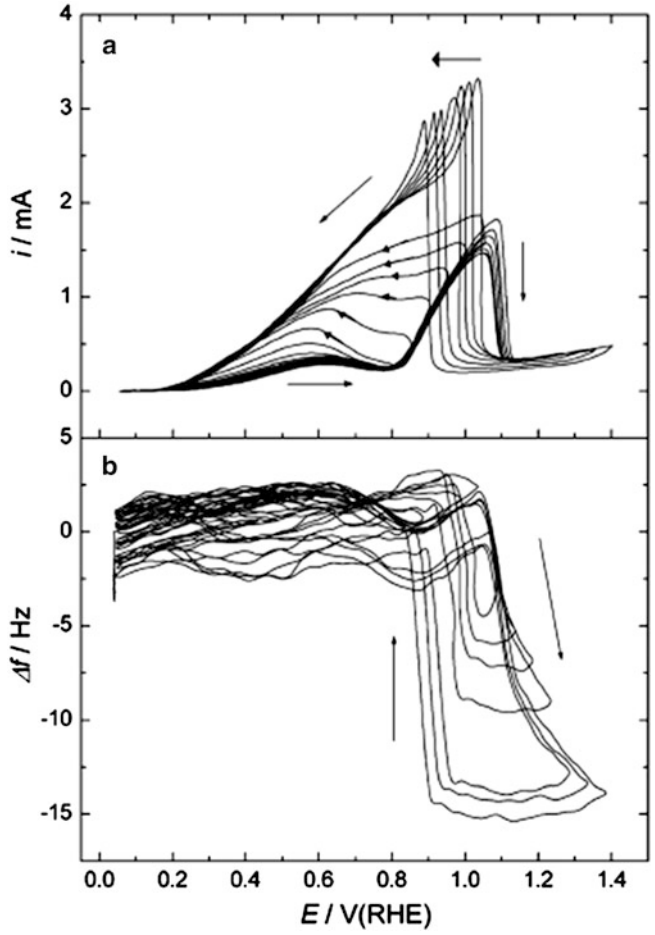


**Fig. 3.10** Cyclic voltammetry using a electrochemical quartz crystal microbalance of formic acid electrooxidation on a polycrystalline Pt surface in 0.2 M formic acid and 0.2 M $HClO_4$ at 50 mV $s^{-1}$ (**a**) current and (**b**) frequency (corresponding to negative mass changes) response. The upper potential limit is sequentially increased with each subsequent cycle [66]

upper potential limits, the subsequent formic acid anodic spike decreases in intensity and is negatively shifted.

### *3.6.2 Desorbed Product Detection*

Several research groups have used differential electrochemical mass spectroscopy (DEMS) to monitor product conversion during formic acid electrooxidation [2, 21, 37, 86–88]. In Fig. 3.2, the origins of the $CO_2$ product formation pathway is investigated by using isotopically labeled formic acid [37].

### 3.6.3 Direct Catalyst Surface Analysis

The in situ study in electrochemical cells of the catalyst surface is challenging due to low surface sensitivity through the electrolyte. Several surface-sensitive techniques have been employed to probe the abundance and/or state of adsorbed surface species formed during formic acid electrooxidation: broadband sum frequency generation [89, 90], surface-enhanced Raman spectroscopy [21], scanning tunneling microscopy [91], and Fourier transform infrared spectroscopy [19, 26, 27, 31, 32, 41, 92–99].

*Fourier transform infrared spectroscopy* (FTIR) is a powerful technique to probe real-time adsorbed surface species (reactants, intermediates, products) and solution constituents due to selected molecular dipole bond vibrations induced by tuned incident radiation [100]. FTIR has been used to study the formic acid electrooxidation reaction mechanism in situ by stepping or scanning the potential where species of interest are generated, from either high potentials where the intermediate species are completely oxidized (a clean surface, >1 V vs. RHE) or low potentials where the intermediate species approaches the coverage limit (blocked surface, <0.05 V vs. RHE) [100]. The three observed reaction intermediates for formic acid electrooxidation are linearly bonded $CO_L$, bridge-bonded $CO_B$, and bridge-bonded formate ($HCOO_{ad}$) with vibrational bands at 2,052–2,080 $cm^{-1}$, 1,810–1,850 $cm^{-1}$, and 1,320 $cm^{-1}$, respectively [27, 98]. The vibration frequencies of the adsorbates are influenced by the electronic characteristics and electrochemical potential of the electrode surface. Additional peaks of lesser intensity are observed for the water adlayer and sulfate/bisulfate at the electrode interface [27, 98].

The initial studies in this area were done in external infrared reflection adsorption spectroscopy (IRAS) mode [26, 41, 92–97], where the incident beam was passed through an optical window, a 1–100 μm ultra thin solution layer, then reflected off the electrode where it transverses back through the aforementioned layers at an incident angle to a detector. The solution layer is minimized to reduce solution interference at the expanse of induced mass transport effects. To enhance surface sensitivity and alleviate mass transport restrictions, attenuated total reflection surface-enhanced infrared adsorption spectroscopy (ATR-SEIRAS) has been used [19, 27, 31, 32, 98, 99]. The radiation passes through the backside of a hemicylindrical Si prism that has a metal film on the front to act as the working electrode and the incident infrared radiation goes to a detector [33, 101].

Considering the work by Pang et al., they clearly demonstrate the positive impact of antimony (Sb) adatoms on Pt for enhanced formic acid electrooxidation; see Fig. 3.11 [27]. They studied a surface coverage of 60 % Sb ($\theta_{Sb} = 0.6$) on polycrystalline Pt in 0.5 M $H_2SO_4$ and 0.1 M formic acid at 10 mV $s^{-1}$ versus RHE. Figure 3.11a shows the normal current response for formic acid electrooxidation on polycrystalline Pt with the corresponding detection of the extent of coverage of the surface by reaction intermediates, $CO_L$, $CO_B$, and formate. At low potentials in the positive potential scan, $CO_L$ is the dominant surface species, with negligible current

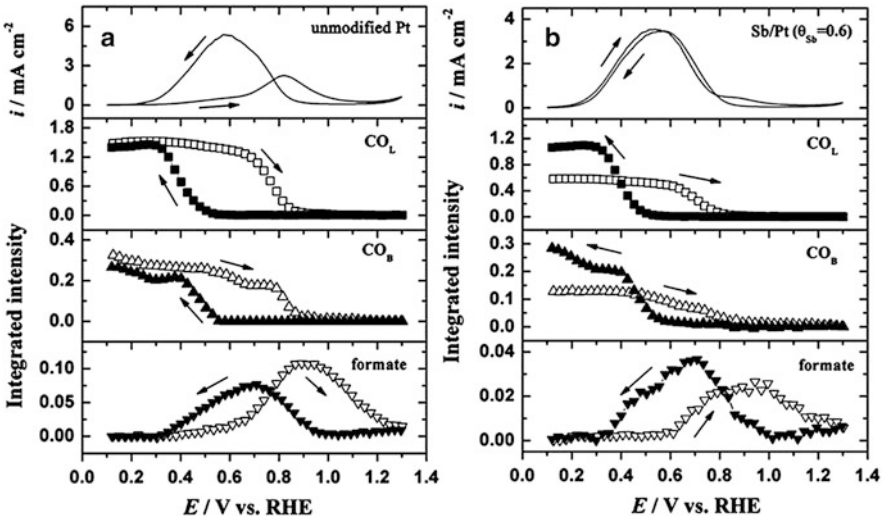


**Fig. 3.11** A time-resolved series of selected ART-FTIR integrated peak intensities as measured during potential cycling on (**a**) polycrystalline Pt and (**b**) 60 % antimony (Sb) adatom covered polycrystalline Pt in 0.5 M $H_2SO_4$ and 0.1 M formic acid at 10 mV $s^{-1}$. From the top-down the series of plots are as follows: the current response, $CO_L$, $CO_B$, and formate [27]

generation. As $CO_{ads}$ is removed from the surface at potentials >0.4 V, the current increases slightly and formate begins to appear on the surface. Above 0.7 V both $CO_{ads}$ species are rapidly removed from the surface and the current increases. In the reverse negative potential scan, the asymmetric current profile has increased and shifted toward lower potentials; the $CO_L$ and $CO_B$ are not detected until the potential is decreased below 0.55 V. Conversely, the Sb-modified surface (Fig. 3.11b) exhibits a symmetric current profile with favorably intensity shifted to lower potentials. The initial $CO_L$ and $CO_B$ intensities at 100 mV are reduced by at least 50 %. The initial rise in current is unaffected by the presence of $CO_{ads}$ and simultaneously decreases with $CO_{ads}$ desorption due to surface oxidation. This observation clearly demonstrates the dominance of the dehydrogenation (direct) pathway on an Sb-modified Pt surface. The rise in $CO_L$ and $CO_B$ intensities in the reverse scan is potentially linked with loss of Sb due to oxidation at elevated potentials.

## 3.7 Conclusions

The type, structure, and electron density clearly determine the reactivity of a catalyst toward formic acid electrooxidation. The catalyst characteristics that promote reactant adsorption in the CH-down orientation exhibit enhanced activity through the dehydrogenation reaction pathway. Pd catalyst initially favors the dehydrogenation pathway but suffers for 30 % activity loss within only 3 h of continuous operation due to accumulation of reaction intermediates on the surface.

A smaller percentage of Pt surface sites participate in the dehydrogenation pathway, limiting activity to high overpotentials that promote $OH_{ads}$ formation to complete the dehydration reaction.

Size of the Pt and Pd catalyst plays an important role in catalytic activity, due to reduction in the abundance of contiguous surface sites and crystallographic facets as the size of nanoparticles are reduced. Geometrically, the reduction in contiguous Pt sites enhances reactivity, with an optimal size of 2 nm. Alternatively, for Pd as the particle size decrease the abundance of unfavorable oxidation states increase, adversely impacting reactivity; the optimal size at 0.4 V is 6.5 nm.

Separate modeling efforts have evolved to include solvation, electronic alterations in the d-band center, and the third-body effect. The findings suggest a combination of a positive electronic shift in the d-band center and third-body effect promotes the dehydration pathway. There exists a need for a cohesive hybrid model that also includes nanoparticle attributes.

## References

1. Gasteiger HA, Garche J (2008) Fuel cells. In: Ertl G (ed) Handbook of heterogeneous catalysis, 2nd edn. Weinheim, Wiley-VCH, pp 3081–3121
2. Weber M, Wang JT, Wasmus S, Savinell RF (1996) Formic acid oxidation in a polymer electrolyte fuel cell. J Electrochem Soc 143:L158–L160
3. Ha S, Rice CA, Masel RI, Wieckowski A (2002) Methanol conditioning for improved performance of formic acid fuel cells. J Power Sources 112:655–659
4. Rice C, Ha S, Masel RI, Waszczuk P, Wieckowski A (2002) Characteristics of formic acid fuel cells. In: Proceedings of the 40th power sources conference, pp 254–257
5. Rice C, Ha S, Masel RI, Waszczuk P, Wieckowski A, Barnard T (2002) Direct formic acid fuel cells. J Power Sources 111:83–89
6. Waszczuk P, Barnard TM, Rice C, Masel RI, Wieckowski A (2002) A nanoparticle catalyst with superior activity for electrooxidation of formic acid. Electrochem Commun 4:732
7. Masel RI, Rice CA, Waszczuk P, Wieckowski A (2003) Fuel cells and fuel cells catalysts. US Patent 7,132,188
8. McGovern MS, Garnett EC, Rice C, Masel RI, Wieckowski A (2003) Effects of Nafion as a binding agent for unsupported nanoparticle catalysts. J Power Sources 115:35–39
9. Rhee Y-W, Ha SY, Masel RI (2003) Crossover of formic acid through Nafion membranes. J Power Sources 117:35–38
10. Rice C, Ha S, Masel RI, Wieckowski A (2003) Catalysts for direct formic acid fuel cells. J Power Sources 115:229–235
11. Uhm S, Lee HJ, Lee J (2009) Understanding underlying processes in formic acid fuel cells. Phys Chem Chem Phys 11:9326–9336
12. Wang X, Hu J-M, Hsing IM (2004) Electrochemical investigation of formic acid electro-oxidation and its crossover through a Nafion membrane. J Electroanal Chem 562:73–80
13. Masel RI (2012) Novel catalyst mixtures for electrochemical conversion of carbon dioxide to formic acid. US Patent Application WO2012006240A1
14. Law WL, Platt AM, Wimalaratne PDC, Blair SL (2009) Effect of organic impurities on the performance of direct formic acid fuel cells. J Electrochem Soc 156:B553–B557
15. Parsons R, VanderNoot T (1988) The oxidation of small organic molecules: a survey of recent fuel cell related research. J Electroanal Chem Interfacial Electrochem 257:9–45

16. Jarvi TD, Stuve EM (1998) Fundamental aspects of vacuum and electrocatalytic reactions of methanol and formic acid on platinum surfaces. In: Lipkowski J, Ross PN (eds) Electrocatalysis. Wiley-VCH, New York, NY, pp 75–133
17. Vielstich W (2003) CO, formic acid, and methanol oxidation in acid electrolytes-mechanisms and electrocatalysis. In: Bard AJ, Stratmann M (eds) Encyclopedia of electrochemistry. Wiley-VCH Verlag GmbH & Co. KGaA, Weinheim, pp 466–511
18. Ross PN Jr (1998) The science of electrocatalysis on bimetallic surfaces. In: Lipkowski J, Ross PN (eds) Electrocatalysis. Wiley-VCH, New York, NY, pp 43–74
19. Chen YX, Heinen M, Jusys Z, Behm RJ (2006) Bridge-bonded formate: active intermediate or spectator species in formic acid oxidation on a Pt film electrode? Langmuir 22: 10399–10408
20. Larsen R, Ha S, Zakzeski J, Masel RI (2006) Unusually active palladium-based catalysts for the electrooxidation of formic acid. J Power Sources 157:78–84
21. Beltramo GL, Shubina TE, Koper MTM (2005) Oxidation of formic acid and carbon monoxide on gold electrodes studied by surface-enhanced Raman spectroscopy and DFT. ChemPhysChem 6:2597–2606
22. Chen S-l, Wu B-l, Cha C-s (1997) An EQCM investigation of oxidation of formic acid at gold electrode in sulfuric acid solution. J Electroanal Chem 431:243–247
23. Chen W, Tang Y, Bao J, Gao Y, Liu C, Xing W, Lu T (2007) Study of carbon-supported Au catalyst as the cathodic catalyst in a direct formic acid fuel cell prepared using a polyvinyl alcohol protection method. J Power Sources 167:315–318
24. Hahn F, Beden B, Lamy C (1986) In situ infrared reflectance spectroscopic study of the adsorption of formic acid at a rhodium electrode. J Electroanal Chem Interfacial Electrochem 204:315–327
25. Wieckowski A, Sobkowski J, Zelenay P (1977) The potential dependence and kinetics of formic acid adsorption on rhodium electrodes. J Electroanal Chem Interfacial Electrochem 84:109–116
26. Gómez R, Weaver MJ (1997) Electrochemical infrared studies of monocrystalline iridium surfaces Part I: Electrooxidation of formic acid and methanol. J Electroanal Chem 435: 205–215
27. Peng B, Wang H-F, Liu Z-P, Cai W-B (2010) Combined surface-enhanced infrared spectroscopy and first-principles study on electro-oxidation of formic acid at Sb-modified Pt electrodes. J Phys Chem C 114:3102–3107
28. Wang H-F, Liu Z-P (2009) Formic acid oxidation at Pt/H2O interface from periodic DFT calculations integrated with a continuum solvation model. J Phys Chem C 113:17502–17508
29. Luo Q, Feng G, Beller M, Jiao H (2012) Formic acid dehydrogenation on Ni(111) and comparison with Pd(111) and Pt(111). J Phys Chem C 116:4149–4156
30. Capon A, Parsons R (1973) The oxidation of formic acid on noble metal electrodes: II A comparison of the behaviour of pure electrodes. J Electroanal Chem Interfacial Electrochem 44:239–254
31. Chen YX, Heinen M, Jusys Z, Behm RJ (2006) Kinetics and mechanism of the electrooxidation of formic acid–spectroelectrochemical studies in a flow cell. Angew Chem Int Ed 45:981–985
32. Samjeske G, Osawa M (2005) Current oscillations during formic acid oxidation on a Pt electrode: insight into the mechanism by time-resolved IR spectroscopy. Angew Chem Int Ed 44:5694–5698
33. Miki A, Ye S, Osawa M (2002) Surface-enhanced IR absorption on platinum nanoparticles: an application to real-time monitoring of electrocatalytic reactions. Chem Commun 14: 1500–1501
34. Beden B, Lamy C (1988) Infrared reflectance spectroscopy. In: Gale RJ (ed) Spectroelectrochemistry: theory and practice. Plenum, New York, NY, p 189
35. Bewick A, Pons B (1985) In: Clark RJH, Hester RE (eds) Advances in infrared and raman spectroscopy. Wiley, Chichester, p 360

36. Watanabe M, Motoo S (1975) Electrocatalysis by ad-atoms: Part II. Enhancement of the oxidation of methanol on platinum by ruthenium ad-atoms. J Electroana Chem Interfacial Electrochem 60:267–273
37. Willsau J, Heitbaum J (1986) Analysis of adsorbed intermediates and determination of surface potential shifts by dems. Electrochim Acta 31:943–948
38. Motoo S, Watanabe M (1980) Electrocatalysis by ad-atoms: Part VII. Enhancement of CO oxidation on platinum by As ad-atoms. J Electroanal Chem Interfacial Electrochem 111:261–268
39. Clavilier J, Parsons R, Durand R, Lamy C, Leger JM (1981) Formic acid oxidation on single crystal platinum electrodes. Comparison with polycrystalline platinum. J Electroanal Chem 124:321–326
40. Adzic RR, Tripkovic AV, O'Grady WE (1982) Structural effects in electrocatalysis. Nature 296:137–138
41. Iwasita T, Xia X, Herrero E, Liess H-D (1996) Early stages during the oxidation of HCOOH on single-crystal Pt electrodes as characterized by infrared spectroscopy. Langmuir 12: 4260–4265
42. Hoshi N, Kida K, Nakamura M, Nakada M, Osada K (2006) Structural effects of electrochemical oxidation of formic acid on single crystal electrodes of palladium. J Phys Chem B 110:12480–12484
43. Benfield RE (1992) Mean coordination numbers and the non-metal-metal transition in clusters. J Chem Soc Faraday Trans 88:1107–1110
44. Park S, Xie Y, Weaver MJ (2002) Electrocatalytic pathways on carbon-supported platinum nanoparticles: comparison of particle-size-dependent rates of methanol, formic acid, and formaldehyde electrooxidation. Langmuir 18:5792–5798
45. Chrzanowski W, Kim H, Wieckowski A (1998) Enhancement in methanol oxidation by spontaneously deposited ruthenium on low-index platinum electrodes. Catal Lett 50:69–75
46. Neurock M, Janik M, Wieckowski A (2008) A first principles comparison of the mechanism and site requirements for the electrocatalytic oxidation of methanol and formic acid over Pt. Faraday Discuss 140:363–378
47. Pavese A, Solis V, Giordano MC (1988) Electrocatalytic oxidation of formic acid on Pd + Pt alloys of different bulk composition in acidic medium. J Electroanal Chem 245(1–2): 145–156
48. Zhou W, Lee JY (2008) Particle size effects in Pd-catalyzed electrooxidation of formic acid. J Phys Chem C 112:3789–3793
49. Pan Y, Zhang R, Blair SL (2009) Anode poisoning study in direct formic acid fuel cells. Electrochem Solid St Lett 12:B23–B26
50. Zhou WP, Lewera A, Larsen R, Masel RI, Bagus PS, Wieckowski A (2006) Size effects in electronic and catalytic properties of unsupported palladium nanoparticles in electrooxidation of formic acid. J Phys Chem B 110:13393–13398
51. Zhou Y, Liu J, Ye J, Zou Z, Ye J, Gu J, Yu T, Yangc A (2010) Poisoning and regeneration of Pd catalyst in direct formic acid fuel cell. Electrochim Acta 55:5024–5027
52. Zhang H-X, Wang S-H, Jiang K, Andre T, Cai W-B (2012) In situ spectroscopic investigation of CO accumulation and poisoning on Pd black surfaces in concentrated HCOOH. J Power Sources 199:165–169
53. Zhu Y, Khan Z, Masel RI (2005) The behavior of palladium catalysts in direct formic acid fuel cells. J Power Sources 139:15–20
54. Jung WS, Han J, Ha S (2007) Analysis of palladium-based anode electrode using electrochemical impedance spectra in direct formic acid fuel cells. J Power Sources 173:53–59
55. Gao W, Keith JA, Anton J, Jacob T (2010) Theoretical elucidation of the competitive electrooxidation mechanisms of formic acid on Pt(1 1 1). J Am Chem Soc 132:18377–18385
56. Leiva E, Iwasita T, Herrero E, Feliu JM (1997) Effect of adatoms in the electrocatalysis of HCOOH oxidation. A theoretical model. Langmuir 13:6287–6293

57. Demirci UB (2007) Theoretical means for searching bimetallic alloys as anode electrocatalysts for direct liquid-feed fuel cells. J Power Sources 173:11–18
58. Babu PK, Kim HS, Chung JH, Oldfield E, Wieckowski A (2004) Bonding and motional aspects of CO adsorbed on the surface of Pt nanoparticles decorated with Pd. J Phys Chem B 108:20228–20232
59. Lu G-Q, Crown A, Wieckowski A (1999) Formic acid decomposition on polycrystalline platinum and palladized platinum electrodes. J Phys Chem B 103:9700–9711
60. Spendelow JS, Wieckowski A (2004) Noble metal decoration of single crystal platinum surfaces to create well-defined bimetallic electrocatalysts. Phys Chem Chem Phys 6: 5094–5118
61. Yin M, Huang Y, Lv Q, Liang L, Liao J, Liu C, Xing W (2011) Improved direct electrooxidation of formic acid by increasing Au fraction on the surface of PtAu alloy catalyst with heat treatment. Electrochim Acta 58:6–11
62. Zhang S, Shao Y, Yin G, Lin Y (2010) Facile synthesis of PtAu alloy nanoparticles with high activity for formic acid oxidation. J Power Sources 195:1103–1106
63. Park I-S, Lee K-S, Yoo SJ, Cho Y-H, Sung Y-E (2010) Electrocatalytic properties of Pd clusters on Au nanoparticles in formic acid electro-oxidation. Electrochim Acta 55: 4339–4345
64. Mazumder V, Lee Y, Sun S (2010) Recent development of active nanoparticle catalysts for fuel cell reactions. Adv Funct Mater 20:1224–1231
65. Lovic JD, Tripkovic AV, Gojkovic SL, Popovic KD, Tripkovic DV, Olszewski P, Kowal A (2005) Kinetic study of formic acid oxidation on carbon-supported platinum electrocatalyst. J Electroanal Chem 581:294–302
66. Tian M, Conway BE (2008) Electrocatalysis in oscillatory kinetics of anodic oxidation of formic acid: At Pt; nanogravimetry and voltammetry studies on the role of reactive surface oxide. J Electroanal Chem 616:45–56
67. Haan JL, Masel RI (2009) The influence of solution pH on rates of an electrocatalytic reaction: formic acid electrooxidation on platinum and palladium. Electrochim Acta 54: 4073–4078
68. Masel RI, Zhu Y, Khan Z, Man M (2006) Low contaminant formic acid fuel for direct liquid fuel cell. US Patent 20060059769
69. Yu X, Pickup PG (2011) Carbon supported PtBi catalysts for direct formic acid fuel cells. Electrochim Acta 56:4037–4043
70. Yu X, Pickup PG (2010) Pb and Sb modified Pt/C catalysts for direct formic acid fuel cells. Electrochim Acta 55:7354–7361
71. Kristian N, Yu Y, Gunawan P, Xu R, Deng W, Liu X, Wang X (2009) Controlled synthesis of Pt-decorated Au nanostructure and its promoted activity toward formic acid electro-oxidation. Electrochim Acta 54:4916–4924
72. Lu Y, Chen W (2012) PdAg alloy nanowires: facile one-step synthesis and high electrocatalytic activity for formic acid oxidation. ACS Catal 2:84–90
73. Liu Z, Guo B, Tay SW, Hong L, Zhang X (2008) Physical and electrochemical characterizations of PtPb/C catalyst prepared by pyrolysis of platinum(II) and lead(II) acetylacetonate. J Power Sources 184:16–22
74. Maxakato NW, Ozoemena KI, Arendse CJ (2010) Dynamics of electrocatalytic oxidation of ethylene glycol, methanol and formic acid at MWCNT platform electrochemically modified with Pt/Ru nanoparticles. Electroanalysis 22:519–529
75. Seland F, Tunold R, Harrington DA (2008) Impedance study of formic acid oxidation on platinum electrodes. Electrochim Acta 53:6851–6864
76. Suo Y, Hsing IM (2009) Size-controlled synthesis and impedance-based mechanistic understanding of Pd/C nanoparticles for formic acid oxidation. Electrochim Acta 55:210–217
77. Uhm S, Chung ST, Lee J (2008) Characterization of direct formic acid fuel cells by impedance studies: in comparison of direct methanol fuel cells. J Power Sources 178:34–43

78. Kang Y, Ren M, Yuan T, Qiao Y, Zou Z, Yang H (2010) Effect of Nafion aggregation in the anode catalytic layer on the performance of a direct formic acid fuel cell. J Power Sources 195:2649–2652
79. Kang S, Lee J, Lee JK, Chung S-Y, Tak Y (2006) Influence of Bi modification of pt anode catalyst in direct formic acid fuel cells. J Phys Chem B 110:7270–7274
80. Conway BE (2003) Electrochemical capacitors their nature, function, and applications. Electrochemistry Encyclopedia. http://electrochem.cwru.edu/encycl/art-c03-elchem-cap.htm
81. Chung S-Y, Uhm S-H, Lee J-K, Kang S-J, Tak Y-S, Lee J-Y (2007) Electrocatalytic oxidation of HCOOH on Pt-based anodes. J Ind Eng Chem 13:339–344
82. Inzelt G, Kertesz V (1996) Effect of poly(aniline) pseudocapacitance on potential and EQCM frequency oscillations arising in the course of galvanostatic oxidation of formic acid on platinum. Electrochim Acta 42:229–235
83. Uhm S, Yun Y, Tak Y, Lee J (2005) EQCM analysis of Bi oxidation mechanism on a Pt electrode. Electrochem Commun 7:1375–1379
84. Hepel M (1999) Electrode-solution interface studies with electrochemical quartz-crystal nanobalance. In: Wieckowski A (ed) Interfacial electrochemistry: theory, experiment, and applications. Marcel Dekker, Inc., Postdam
85. Jerkiewicz G, Vatankhah G, S-i T, Lessard J (2011) Discovery of the potential of minimum mass for platinum electrodes. Langmuir 27:4220–4226
86. Casado-Rivera E, Gal Z, Angelo ACD, Lind C, DiSalvo FJ, Abruna HD (2003) Electrocatalytic oxidation of formic acid at an ordered intermetallic PtBi surface. ChemPhysChem 4:193–199
87. Miura A, Wang H, Leonard BM, Abruna HD, Di SFJ (2009) Synthesis of intermetallic PtZn nanoparticles by reaction of Pt nanoparticles with Zn vapor and their application as fuel cell catalysts. Chem Mater 21:2661–2667
88. Xia XH, Iwasita T (1993) Influence of underpotential deposited lead upon the oxidation of formic acid in perchloric acid at platinum electrodes. J Electrochem Soc 140:2559–2565
89. Behrens RL, Lagutchev A, Dlott DD, Wieckowski A (2010) Broad-band sum frequency generation study of formic acid chemisorption on a Pt (1 0 0) electrode. J Electroanal Chem 649:32–36
90. Behrens RL, Wieckowski A (2009) Electrochemical and spectroscopic studies of small organic molecule oxidation on low index platinum electrodes. Central Regional Meeting of the American Chemical Society, Cleveland, OH
91. Rodriguez-Lopez J, Bard AJ (2010) Scanning electrochemical microscopy: surface interrogation of adsorbed hydrogen and the open circuit catalytic decomposition of formic acid at platinum. J Am Chem Soc 132:5121–5129
92. Chang SC, Leung LWH, Weaver MJ (1990) Metal crystallinity effects in electrocatalysis as probed by real-time FTIR spectroscopy: electrooxidation of formic acid, methanol, and ethanol on ordered low-index platinum surfaces. J Phys Chem 94:6013–6021
93. Yang Y-Y, Zhou Z-Y, Sun S-G (2001) In situ FTIRS studies of kinetics of HCOOH oxidation on Pt(110) electrode modified with antimony adatoms. J Electroanal Chem 500:233–240
94. Beden B, Bewick A, Lamy C (1983) A study by electrochemically modulated infrared reflectance spectroscopy of the electrosorption of formic acid at a platinum electrode. J Electroanal Chem Interfacial Electrochem 148:147–160
95. Lamy C, Leger JM (1991) Electrocatalytic oxidation of small organic molecules at platinum single crystals. J Chim Phys Phys -Chim Biol 88:1649–1671
96. Arenz M, Stamenkovic V, Ross PN, Markovic NM (2004) Surface (electro-)chemistry on Pt (111) modified by a pseudomorphic Pd monolayer. Surf Sci 573:57–66
97. Arenz M, Stamenkovic V, Schmidt TJ, Wandelt K, Ross PN, Markovic NM (2003) The electro-oxidation of formic acid on Pt–Pd single crystal bimetallic surfaces. Phys Chem Chem Phys 5:4242–4251
98. Chen YX, Ye S, Heinen M, Jusys Z, Osawa M, Behm RJ (2006) Application of in-situ attenuated total reflection-fourier transform infrared spectroscopy for the understanding of

complex reaction mechanism and kinetics: formic acid oxidation on a Pt film electrode at elevated temperatures. J Chem Phys B 110:9534–9544
99. Samjeske G, Miki A, Ye S, Osawa M (2006) Mechanistic study of electrocatalytic oxidation of formic acid at platinum in acidic solution by time-resolved surface-enhanced infrared absorption spectroscopy. J Chem Phys B 110:16559–16566
100. Bard AJ, Faulkner LR (2006) Electrochemical methods: fundamentals and applications. Wiley, New York
101. Miki A, Ye S, Senzaki T, Osawa M (2004) Surface-enhanced infrared study of catalytic electrooxidation of formaldehyde, methyl formate, and dimethoxymethane on platinum electrodes in acidic solution. J Electroanal Chem 563:23–31